# EXPERIMENTAL VERIFICATION ON CAGING-CAPTURE OF A FREE-FLOATING OBJECT BY A DUAL-ARM SPACE ROBOT

Virtual Conference 19-23 October 2020

Tomoya Matsushita[1], Kazuya Yoshida[1]

[1] *Department of Aerospace Engineering, Tohoku University, Aoba 6-6-01, Aramaki, Aoba-ku, Sendai, Miyagi, Japan,*
*Email: tomoya.matsushita.s5@dc.tohoku.ac.jp, yoshida@astro.mech.tohoku.ac.jp*

## ABSTRACT

One proposed space debris removal method is the utilization of a robotic arm mounted on a chaser satellite. In general, to achieve a successful robotic capture, force sensor feedback is effective; unfortunately such sensors increase the weight and level of complexity of the spacecraft. For this reason, we suggest a space debris removal method utilizing a dual-arm space robot with capture control via caging. "Caging" is an idea to geometrically restrict an object by using robotic manipulators or fingers. In this paper, we demonstrate the successful caging capture of a free-floating target and evaluate the caging condition using the object closure model. The proposed caging capture algorithm was validated by experiments using a dual-arm free-floating robot testbed.

## 1 INTRODUCTION

Be it from historical rocket stages, malfunctioning satellites or recent orbital collisions, the amount of Earth orbital debris is increasing rapidly[1]. As orbital velocities are quite high, the amount of energy involved in an orbital collision is immense; the potential of future collisions or collision fragmentation threaten working spacecraft. It becomes necessary to promote active space debris capture and deorbiting missions. In general, space debris can be classified as non-cooperative (without attitude control and noncommunicative) and must be securely detumbled and captured for a successful mission. Hereafter, the space debris to be captured will be referred to as a target.

One active removal method is robotic manipulator capture; manipulator capture advantages include precision control and manipulation of the target thanks to their stiff composites[2]. The capturing phase involves physical interception and thus is highly risky when the impact is large[3]. X. Cyril et al.[4] presented the importance of determining the conditions of impact upon a flexible-link free-floating space robot. Since the impact occurs in a short time, it is difficult to sense and control the contact force. H. Nakanishi et al.[5] proposed the virtual mass of impedance system (VMI) model to clarify the condition of maintaining the contact and preventing the robot pushing the target beyond the manipulator reach based on contact dynamics. These past works assume that mass and moment of inertia of the target are fully known. In general, to enable capture of a free-flying robot with a robotic manipulator, force sensor feedback control, knowledge of the target's mass, and knowledge of the target's inertial properties are required. However, it is quite difficult to acquire mass and inertial properties in space from a non-cooperative target.

Therefore, a dual-arm robotic system is proposed here. When mass and inertia are unknown, a single manipulator arm may accidentally induce additional undesired motion whereas a second manipulator may be able to compensate for or counteract said undesired motion. As related work, S. Liu et al.[6] presented the control of a flexible dual-arm space robot capturing an object. The dynamics model of the robot system was derived with the Lagrangian formulation. R. Takahashi et al.[7] demonstrated a detumbling and capture of a spinning target by a dual-arm robot, based on a hybrid simulator; the robot base was fixed on the ground and was not free-floating. K. Nagaoka et al.[8] demonstrated the repeated-impact based capture by a dual-arm space robot both computationally and experimentally. They presented the feasibility of a repeated-impact based method without precise force sensor feedback control. Moreover, the whole system was free-floating. However, the robot only had one contact tip on each arm and the shape of the target was limited to a cylinder type. Hence, we introduced a caging-based method. "Caging" refers to the geometric restriction of an object by using multiple robots or a multi-fingered robotic manipulator[9]. We propose that the caging capture method makes it possible to capture non-axisymmetric targets such as cubes, rectangular prisms, and other polyhedrons.

This paper is organized in 6 sections as follows. Section 2 showcases a model of the target capture by a dual-arm space robot. The dual-arm robot equations of motion are also introduced there. Section 3 details the cap-
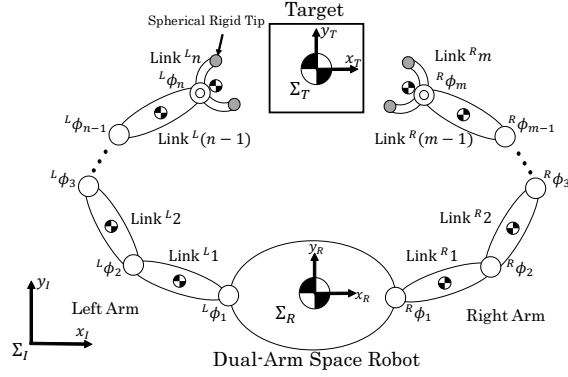
*Figure 1 : Target Capture Model by a Dual-Arm Space Robot*

ture control method based on the proposed model. Section 4 exhibits the developed 2-dimensional microgravity testbed. Section 5 shows the experimental results and validation of the proposed capture method. The caging capture metric (the object closure condition) is discussed there. Finally, section 6 summarizes the contributions of this paper.

## 2   DUAL-ARM SPACE ROBOT

### 2.1   Target Capture Model

A 2-dimensional schematic view of a dual-arm chaser robot and a target is shown in Fig. 1. with respect to this configuration, the following experimental conditions are defined:

- The chaser robot is composed of a base and serial link arms

- Each arm has a forked end effector with a passive (non actuated) joint and spring-damper mounted contact compliances

- Target mass and moment of inertia are unknown

- The target is a single rigid body with a square shape

- The size and shape of the target is known and the 3DoF position and attitude of the target is measured

The following experimental assumptions are defined:

- Gravitational acceleration is zero

- The chaser base, arm links, joints, and target are rigid

- Contact only occurs between the end effector and the target

- Contact is limited to point contacts; contact force and torque are generated at only the contact point

### 2.2   Dual-Arm Space Robot Equations of Motion

For the dual-arm model, the superscript $k$ in the upper left of each variable indicates that the said arm is left(L) or right(R). The key variables used in the robot model are defined as follows.

$H_b \in R^{6 \times 6}$ : Inertia matrix of the robot base
$^k H_m \in R^{n^k \times n^k}$ : Inertia matrix of the arm $k$
$^k H_{bm} \in R^{6 \times n}$ : Interference inertia matrix of the base and the arm $k$
$x_b \in R^6$ : Center of mass position of the base
$^k \phi \in R^{n^k}$ : Joint angle of the arm $k$
$c_b \in R^6$ : Velocity nonlinear term of the base
$^k c_m \in R^{n^k}$ : Velocity nonlinear term of the arm $k$
$F_b \in R^6$ : External force applied on the base
$^k \tau \in R^{n^k}$ : Torque applied on the joint of the arm $k$
$^k J_b \in R^{6 \times 6}$ : Jacobian matrix of the base
$^k J_m \in R^{6 \times n^k}$ : Jacobian matrix of the arm $k$
$^k F_h \in R^6$ : External force applied on the tip of the arm $k$

Unless otherwise specified, each variable is defined in the inertial coordinate system $\Sigma_I$. Using the variables above, the dual-arm space robot equations of motion are introduced as follows[10]:

$$
\begin{bmatrix} H_b & {}^L H_{bm} & {}^R H_{bm} \\ {}^L H_{bm}^T & {}^L H_m & \mathbf{0}_{L_n \times R_n} \\ {}^R H_{bm}^T & \mathbf{0}_{L_n \times R_n}^T & {}^R H_m \end{bmatrix} \begin{bmatrix} \ddot{x}_b \\ {}^L \ddot{\phi} \\ {}^R \ddot{\phi} \end{bmatrix} + \begin{bmatrix} c_b \\ {}^L c_m \\ {}^R c_m \end{bmatrix}
$$

$$
= \begin{bmatrix} F_b \\ {}^L \tau \\ {}^R \tau \end{bmatrix} + \begin{bmatrix} {}^L J_b^T & {}^R J_b^T \\ {}^L J_m^T & \mathbf{0}_{6 \times L_n}^T \\ \mathbf{0}_{6 \times R_n}^T & {}^R J_m^T \end{bmatrix} \begin{bmatrix} {}^L F_h \\ {}^R F_h \end{bmatrix} \quad (1)
$$

## 3   TARGET CAPTURE CONTROL

In this section, the specific method to control the end effector velocity and the path tracking algorithm are discussed.

### 3.1   End Effector Velocity Control by Generalized Jacobian Matrix

Generally, the relationship between the end effector velocity and each joint's angular velocity can be expressed by a Jacobian matrix. With respect to space robots, the whole system is free-floating; the base is not fixed to the ground. Accordingly, the velocity of the base must be taken into consideration. Consequently, the Generalized Jacobian matrix[10] was used: an extended Jacobian matrix for a free-flying robot. The relationship
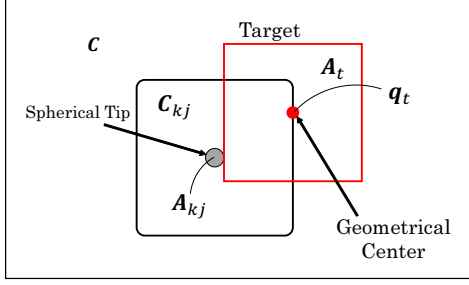
Figure 2 : Capture Sequence



Figure 3 : Calculation of Desired Translational Velocity



Figure 4 : Calculation of Desired Angular Velocity

between end effector velocity and each joint's angular velocity can be expressed as follows with this matrix:

$$\begin{bmatrix} {}^L\dot{\boldsymbol{x}}_h \\ {}^R\dot{\boldsymbol{x}}_h \end{bmatrix} = \boldsymbol{J}^* \begin{bmatrix} {}^L\dot{\boldsymbol{\phi}} \\ {}^R\dot{\boldsymbol{\phi}} \end{bmatrix}$$
$$= \boldsymbol{J}^*\dot{\boldsymbol{\phi}} \qquad (2)$$

By reforming Eq. (2), we obtain the Eq. (3)

$$\dot{\boldsymbol{\phi}} = \boldsymbol{J}^{*+} \begin{bmatrix} {}^L\dot{\boldsymbol{\phi}} \\ {}^R\dot{\boldsymbol{\phi}} \end{bmatrix} \qquad (3)$$

where $\boldsymbol{J}^{*+}$ is the pseudo inverse matrix of $\boldsymbol{J}^*$. Using Eq. (3), end effector velocity can be controlled by the angular velocity of each motor.

### 3.2 Capture Sequence toward Caging

To capture the target, we first assumed that a sufficient condition was to hold opposing corners. The capture sequence was categorized into 4 phases as shown in Fig. 2. The details of each phase are explained as follows:

Phase 1 (Target Motion Estimation Phase)
Firstly, the chaser robot estimated the translational velocity, angular velocity, and orientation of the target. To estimate these properties in a 2DoF system, temporal position data of at least 2 points is required. For this experiment, the data was collected via an externally mounted motion tracking system with a sample rate of 100Hz. The chaser robot obtained the position information from the external system at 100Hz and estimated the target's motion. When $\theta_t$ (target angle) reached 0, the algorithm proceeded to Phase 2.

Phase 2 (End Effector Motion Calculation Phase)
Secondly, the robot calculated the desired velocity to reach the desired position of the end effector in the required time. Here, we define the variables in Fig. 3 as

follows:
$\omega$ : Angular velocity of the target
$v_t$ : Translational velocity of the target
$\theta_t$ : Rotation angle of the target (the angle of $\overrightarrow{PQ}$ with respect to the inertial frame)
$\Delta T$ : Required time that is taken from $\theta_t = 0$ to $\theta_t = \pi/4$
$t_0$ : Time when $\theta_t$ becomes 0
$\boldsymbol{p}_h$ : Initial position of the end effector
${}^d\boldsymbol{p}_h$ : Desired position of the end effector
${}^d\boldsymbol{v}_h$ : Desired velocity of the end effector

When $\theta_t$ reached 0, the on-board computer calculated the desired position and velocity for the end effector. As mentioned previously, the angular velocity of each joint (excepting the end effector joint) was controlled. Thus, the desired velocity as calculated by Eq. (4) is used as the actuation control input. Once the desired end effector velocity is determined, the algorithm proceeded to Phase 3.

$$^d\boldsymbol{v}_h = \frac{^d\boldsymbol{p}_h - \boldsymbol{p}_h}{\Delta T} \qquad (4)$$

Phase 3 (Control and Actuation Phase)
Thirdly, motor actuation began and aimed to have both manipulators reach the desired positions within $\Delta T$. Each end effector's angular velocity was also defined so as to not collide with the target before caging. The desired angular velocity was set as shown in Fig. 4 and Eq. (5). As the time reached $\Delta_T$, the process reached Phase 4.

*Figure 5 : Space Composed by Target and Spherical Tip*

$$d\boldsymbol{\omega}_h = \begin{bmatrix} L_\omega \\ R_\omega \end{bmatrix} = \begin{bmatrix} \dfrac{L_\theta}{\Delta T} \\ \dfrac{R_\theta}{\Delta T} \end{bmatrix} \tag{5}$$

Phase 4 (Caging Phase)
Finally, motor actuation, no longer being required, was stopped and a static closure-condition was achieved. All motor commands ceased in this phase.

### 3.3 Caging State Validation via Object Closure Condition

Caging success can be validated by means of the object closure condition. Once caged, the object has no path from the current position to any given enclosed position that is beyond a specified threshold distance[11]. In this subsection, we discuss the geometric border and the movable domain of the target. Also, a necessary and sufficient condition where caging is established for any arbitrary target angle will be discussed. As observable in Fig. 5, the following variables are defined in configuration space:

$C$ : Free space for the target defined by $A_{kj}$
$A_t$ : Space of the target
$A_{kj}(k = L, R)$ : Space of the j-th spherical tip
$q_t$ : Target geometric center and orientation vector
j-th ($j = 1, 2$) end effector spherical tip obstacle space can be represented as follows:

$$C_{kj} = \{q_t \in C \mid A_t(q_t) \cap A_{kj}(\boldsymbol{\phi}^{kj} \neq \emptyset\} \tag{6}$$

where $\boldsymbol{\phi}^{kj} = \left[\phi_1^k \cdots \phi_m^k\right]^T$ represents the joint angle vector and $m$ defines the link number of each end effector. Additionally, the superscript $k$ in the upper right of each variable indicates that the respective arm is left(L) or right(R)

The union of the obstacle space composed by the end effectors can be expressed as follows:

$$C_{hand} = \bigcup_k \bigcup_{j=1}^{m} C_{kj}(\boldsymbol{\phi}^{kj}) \tag{7}$$

The space $C^{free}$, where the target can move freely can be given as:

$$C^{free} = C \backslash C_{hand} \tag{8}$$

In the composed space $C^{free}$, the set $C_t^{free}$ can be expressed as:

$$q_t \in C_t^{free} \tag{9}$$

In the composed space $C^{free}$, a set $C_{inf}^{free}$ including arbitrary point sets $q_{inf}$ outside the border can be expressed as:

$$q_{inf} \in C_{inf}^{free} \tag{10}$$

When the target cannot escape from the composed space which is separated from the border, there is no path connecting $C_t^{free}$ to $C_{inf}^{free}$. Thus, the condition of object closure can be written as:

$$C_t^{free} \bigcap C_{inf}^{free} = \emptyset \tag{11}$$

Fig. 6 shows a caging achieved state because no path exists for the geometrical center of the target to escape from the space $C_{inf}^{free}$ and object closure is achieved when the target retains its orientation. In contrast, in the composed space as shown in Fig. 7, there is a path to escape from $C_t^{free}$ to $C_{inf}^{free}$. Thus, object closure is constructed, and caging is not achieved under such circumstance.

Here, we derive the caging condition state about the positions between end effector tips and the target for any target's orientation. Fig. 8 shows the state when the target cannot escape to $C_{inf}^{free}$ at its orientation is $\theta_t$. When such a position relationship is created, the path to escape to $C_{inf}^{free}$ is enclosed by the space $C_{L1}$, $C_{L2}$, $C_{R1}$, and $C_{R2}$. When each end effector is fixed in such a position, the target is caged in an any arbitrary posture. Here, we define the distance between the center of the spherical tips $L1 - R2$, $L2 - R1$, $L1 - R1$, $L2 - R2$ as $D^{L1R2}$, $D^{L2R1}$, $D^{L1R1}$, and $D^{L2R2}$, respectively. Also, we define the diameter of the spherical tip as $d$, the length of the target's one side as $l_t$, and the distance between the center of the spherical tips in the same end effector as $l$. Then, the minimum values of $D^{L1R2}$ and $D^{L2R1}$ (which is shown in Fig. 8) are defined as follows:

$$D_{min(\theta_t')}^{L1R2} = D_{min(\theta_t')}^{L2R1} = \frac{d + l_t}{sin(\theta_t')} - \frac{l}{tan(\theta_t')} \tag{12}$$

Here, $\theta_t'$ is defined as:

$$\theta_t' = \begin{cases} \theta_t : & \frac{\pi}{2} < \theta_t \leq \frac{\pi}{4} + \frac{\pi}{2}n \\ \frac{\pi}{2} - \theta_t : & \frac{\pi}{4} + \frac{\pi}{2}n < \theta_t \leq \frac{\pi}{2} + \frac{\pi}{2}n \end{cases} \tag{13}$$
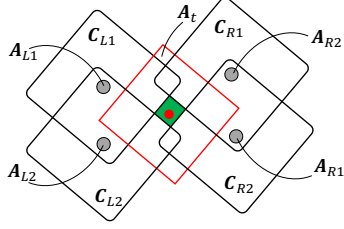
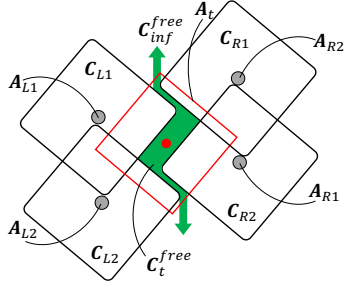*Figure 6 : Closure and Obstacle Space of Caging State*



*Figure 7 : Closure and Obstacle Space of Non-Caging State*

where $n \in \mathbb{Z}$. Also, the minimum values of $D^{L1R1}$ and $D^{L2R2}$ are defined as follows:

$$D_{min}^{L1R1} = D_{min}^{L2R2} = \sqrt{\left\{\frac{d+l_t}{sin(\theta_t')} - \frac{l}{tan(\theta_t')}\right\}^2 + l^2} \quad (14)$$

When there is no target escape path to $C_{inf}^{free}$ as shown in Fig. 9, the target's degree of freedom is limited to zero. From the geometrical relationship, $D_{min}^{L1R2}$ and $D_{min}^{L2R1}$ are expressed as follows when $\theta_t$ is $\pi/4 + n \cdot \pi/2$:

$$D_{min}^{L1R2}\left(\frac{\pi}{4} + \frac{\pi}{2}n\right) = D_{min}^{L2R1}\left(\frac{\pi}{4} + \frac{\pi}{2}n\right) = \sqrt{2}(d+l_t) - l \quad (15)$$

This indicates the minimum values of $D_{min(\theta_t')}^{L1R2}$ and $D_{min(\theta_t')}^{L2R1}$ are the same when $\theta_t$ is $\pi/4$.

Next, we discuss the maximum value of the distance between the spherical tips. The distance in which the target cannot escape to $C_{inf}^{free}$ at an arbitrary orientation $\theta_t$ is expressed as below using a diagonal line of the target's geometry square:

$$D_{max(\theta_t')}^{L1R2} = D_{max(\theta_t')}^{L2R1} = \sqrt{2}(d+l_t)|cos(\theta_t')| \quad (16)$$

$$D_{max(\theta_t')}^{L1R1} = D_{max(\theta_t')}^{L2R2} = \sqrt{\left\{\sqrt{2}(d+l_t)|cos(\theta_t')|\right\}^2 + l^2} \quad (17)$$

Also, $l$ must satisfy the condition $l < \sqrt{2}(d+l_t)|sin(\theta_t')|$. From now on, we assume that $l$ satisfies this inequality.
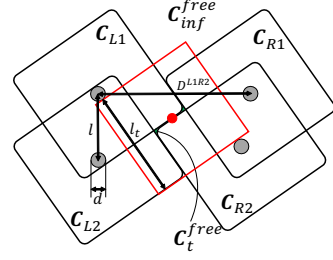


*Figure 8 : Caging State for Minimum Distance Between End Effectors*
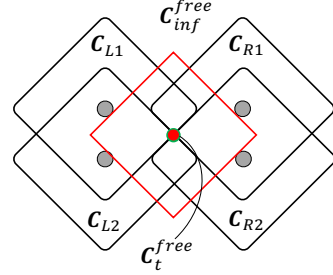


*Figure 9 : Caging State for Minimum Distance Between End Effectors at $\theta_t = \pi/4 + n \cdot \pi/2 (n \in \mathbb{Z})$*

From the above, we consider caging as achieved when all 4 inequalities Eq. (18) are satisfied.

$$\frac{d+l_t}{sin(\theta_t')} - \frac{l}{tan(\theta_t')} < D^{L1R2}(\theta_t') < \sqrt{2}(d+l_t)|cos(\theta_t')|$$

$$\frac{d+l_t}{sin(\theta_t')} - \frac{l}{tan(\theta_t')} < D^{L2R1}(\theta_t') < \sqrt{2}(d+l_t)|cos(\theta_t')|$$

$$\sqrt{\left\{\frac{d+l_t}{sin(\theta_t')} - \frac{l}{tan(\theta_t')}\right\}^2 + l^2} < D^{L1R1}(\theta_t')$$
$$< \sqrt{\left\{\sqrt{2}(d+l_t)|cos(\theta_t')|\right\}^2 + l^2}$$

$$\sqrt{\left\{\frac{d+l_t}{sin(\theta_t')} - \frac{l}{tan(\theta_t')}\right\}^2 + l^2} < D^{L2R2}(\theta_t')$$
$$< \sqrt{\left\{\sqrt{2}(d+l_t)|cos(\theta_t')|\right\}^2 + l^2}$$
$$(18)$$

## 4  EXPERIMENT

### 4.1  Air Bearing Testbed

To demonstrate target caging capture, we developed a dual-arm service robot testbed as shown in Fig. 10. Each arm's end effector had 2 spherical tips mounted to a spring-damper as a mechanical compliance. In this
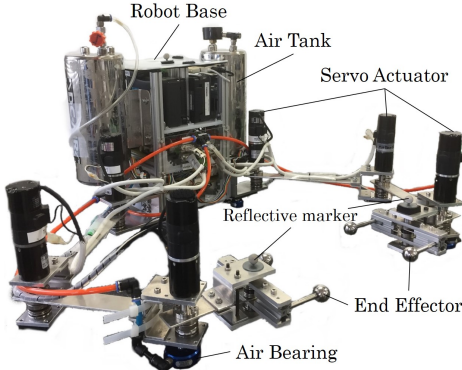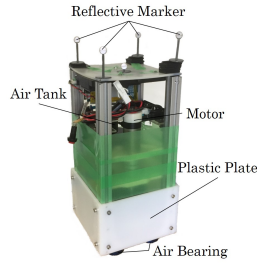
Figure 10 : Dual-Arm Space Robot Testbed
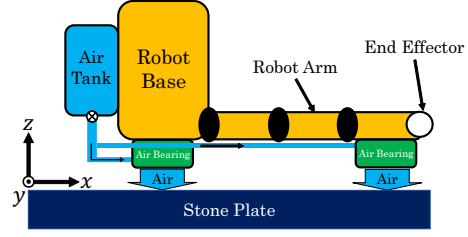


Figure 11 : Target Testbed



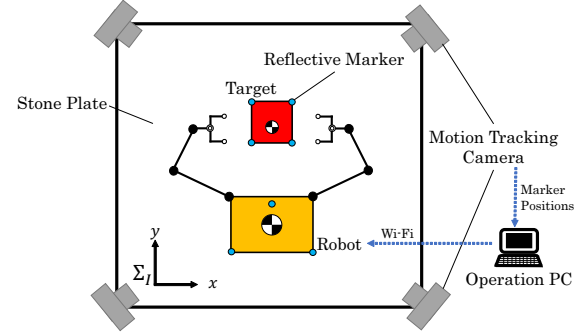Figure 12 : Schematic View of Air Floatation System



Figure 13 : Experiment Environment Configuration

## 4.2 Experimental Conditions

In order to accurately record and analyze the motion of the chaser robot and target, we introduced an externally mounted motion tracking system(OptiTrack FLEX:V100R2; NaturalPoint Inc.) whose sampling frequency was 100Hz. The system consisted of 4 motion tracking cameras, reflective markers, and an operation PC, as shown in Fig. 13. To maintain the free-floating motion, the on-board computer and operational PC were connected via Wi-Fi for remote operation. In this study, we assumed that the approaching phase between the chaser and target had been completed. Also, the deorbit phase was also not taken into consideration here. We began the experiment by putting the target just between the chaser end effectors so as to minimize the relative translational velocity. After that, the testbed air tank's bulb was opened and a command was sent to start the target rotation and the robot control. In this way collision between the end effector and target was avoided. In the experiment, $^R\phi = [-60°\,90°\,60°]$, $^L\phi = [60° - 90° - 60°]$, $\omega_t = 0.9$[rad/s] were set.

manner, the target was caged with 4 contact points. Additionally, the service robot had air tanks and air bearings(S102501 and S104001; NEWWAY Air Bearings) on its bottom surface to minimize friction on a polished granite plane surface and thus simulated a free-flying state, constrained to 2 dimensions as shown in Fig. 12. The captured target is shown in Fig. 11 and was equipped with a similar air bearing system. The target contained a uniaxial driving motor inside its body. The rotational speed of the motor could be set arbitrarily and the target started rotating by the induced reaction-torque from the motor. In the chaser robot base, an on-board computer (PICO-BT01; AAEON Technology Inc.), motor drivers (1XH Power Module; Hibot Corp.), microcontrollers (SH7125; Renesas Electronics Corp.), and Lithium-ion batteries (E-HL9S; IDX Company, Ltd.) were installed. In the manipulator arms, DC servo actuators (RH8D-3006-E100AL; Harmonic Drive Systems, Inc.) and a built-in incremental encoder was mounted on each actuator. These 3 actuators gave 3 DOF to each arm so that the end effector could control translational velocities ($x$ and $y$ direction) and angular velocity. Parameter details are shown in Tab. 1. The Link$^k$1 was connected to the chaser base and Link$^k$3 included the end effector. $l_h$, $l_v$, and $l_t$ refer to the horizontal, vertical length of the chaser base and length of a side of the target, respectively.

Table 1 : Parameters of the Testbeds

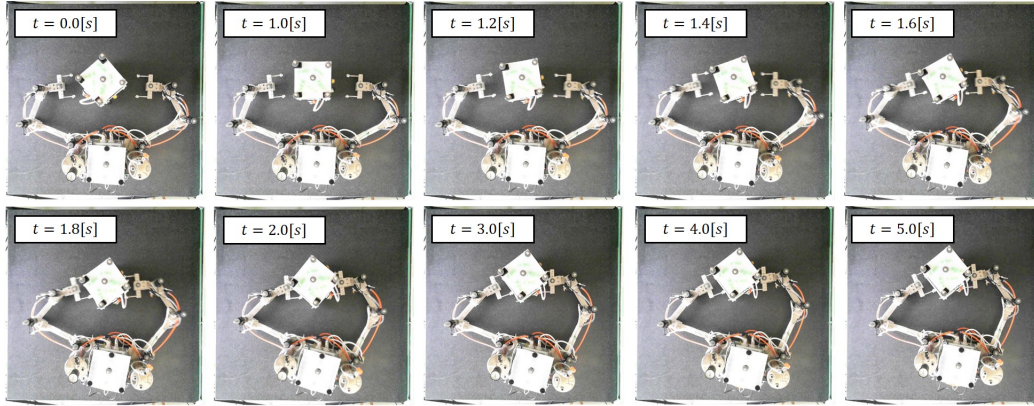|  | Mass[kg] | Inertia[kg·m$^2$] | Length[m] |
|---|---|---|---|
| Base | 7.70 | 0.0978 | $l_h$=0.32 $l_v$=0.15 |
| Link$^{R,L}$1 | 1.09 | 0.00371 | 0.25 |
| Link$^{R,L}$2 | 0.98 | 0.00149 | 0.18 |
| Link$^{R,L}$3 | 0.32 | 0.000752 | 0.095 |
| Target | 4.45 | 0.0172 | $l_t$=0.15 |

Figure 14 : Snapshots of Experimental Results
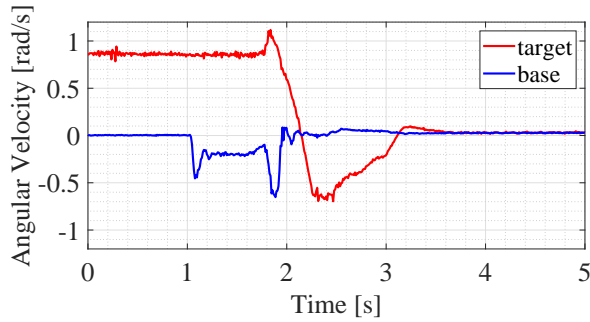


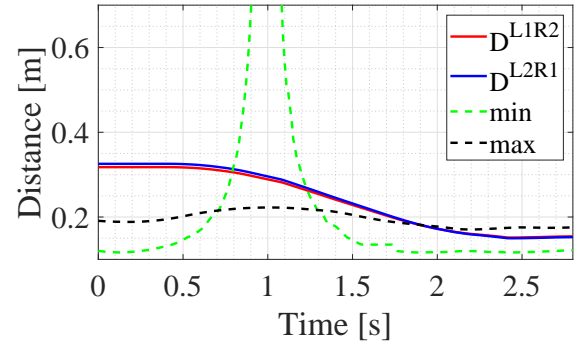Figure 15 : Time History of Angular Velocity of the Target and Robot Base

## 5   RESULT AND DISCUSSION

Following the control method, evaluation method, and experimental conditions, this section presents the experiment results and describes the caging validation. These results verify the fundamental feasibility of the suggested capture method.

### 5.1   Capture Experiment

The snapshots of the capture experiment are shown in Fig. 14. It was confirmed that the arm's manipulation began at $t = 1.0$[s] (thus defining the start of Phase 2). Then, the caging state was created at approximately $t = 2.0$[s] and the motor actuation ceased. The relative position and orientation of both arms were fixed with respect to the chaser base coordinate system. Fig. 15 shows the time history of the angular velocity of the robot base and target. When $t = 1.8$[s], the first collision occurred and the angular velocity of the target was attenuated. When $t = 3.6$[s], detumbling had been completed and it was confirmed that the angular velocity of the chaser base and target converged to a steady state. From these figures, it is apparent that the capture experiment was successful. In the next subsection, the result
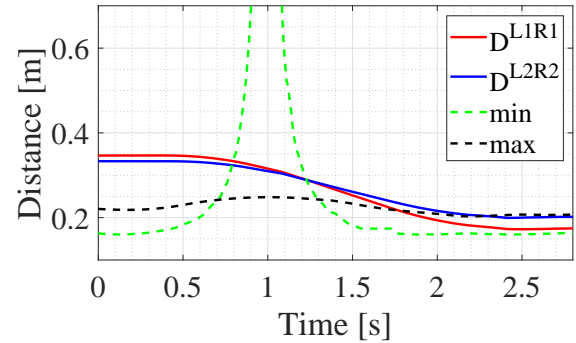


Figure 16 : Time History of Distance between End Effector L1-R2 and L2-R1



Figure 17 : Time History of Distance between End Effector L1-R1 and L2-R2

is quantified from the viewpoint of object closure.

### 5.2   Verification by Object Closure

Fig. 16 shows the time history of $D^{L1R2}, D^{L1R2}$ and $D^{L1R2}_{max(\theta'_t)}, D^{L1R2}_{min(\theta'_t)}$ which were defined in section 3. Fig. 17 also shows the time history of $D^{L1R1}, D^{L2R2}$ and $D^{L1R1}_{max(\theta'_t)}, D^{L2R2}_{min(\theta'_t)}$. From these figures, it is confirmed that the inequalities as shown in Eq. (18) were satisfied as of $t = 2.0$[s]. The object closure condition was

achieved and it was established that the target could not escape from the free space even by adopting any arbitrary angle $\theta_t$.

# 6 CONCLUSIONS

The conclusions of this paper are summarized as follows:

- We demonstrated a caging capture of a free-floating object by a dual-arm space robot.

- We discussed the object closure condition to quantify the caging state.

- We provided evidence of the fundamental feasibility of caging capture without force sensing for active space debris removal missions.

- We demonstrated the validity of the proposed algorithm by experiments with a spinning non-axisymmetric target in the squared shape using a free-floating testbed.

These observations indicate that there exists the potential for debris removal spacecraft to be made simpler and lighter by means of adopting a caging capture approach early on in the design phase.

As the next step of this study, an on-board sensing device to determine the target information such as geometry and inertial state will be pursued; an external ($3^r d$ person) motion tracking system is likely not feasible in space. We demonstrated that if some characteristic points such as the corner of the target are known, the detumbling and capture were achievable. In order to apply this theory to real space robot applications, a real-time target detection device must be developed based on image processing, machine vision technologies, and so on.

Also, a 3-dimensional caging capture study should be conducted; robot and target motion in 3-dimensions is complex and challenging. Due to the challenges of recreating a 3-dimensional microgravity environment, it may be desirable to pursue such research through computer simulation.

## References

[1] ESA Space Debris Office, 'ESA's Annual Space Environment Report', *GEN-DB-LOG-00271-OPS-SD*, July, 2019.

[2] M. Shan, J. Guo, and E. Gill, 'Review and comparison of active space debris capturing and removal methods', *Progress in Aerospace Sciences*, Vol. 80, pp. 18-32, January, 2019.

[3] A. Flores-Abad, O. Ma, K. Pham, and S. Ulrich, 'A review of space robotics technologies for on-orbit servicing', *Progress in Aerospace Sciences*, Vol. 68, pp. 1-26, July, 2014.

[4] X. Cyril, G. Jaar, and A. Misra, 'The effect of payload impact on the dynamics of a space robot', *Proceedings of the 1993 IEEE/RSJ International Conference on Intelligent Robots and Systems*, pp. 2070-2075, 1993.

[5] H. Nakanishi, N. Uyama, and K. Yoshida, 'Virtual Mass of Impedance System for Free-Flying Target Capture', *Proceedings of the 2010 IEEE/RSJ International Conference on Intelligent Robots and Systems*, pp. 4101-4106, 2010.

[6] S. Liu, L. Wu, and Z. Lu 'Impact dynamics and control of a flexible dual-arm space robot capturing an object', *Applied Mathematics and Computation*, Vol. 185, pp. 1149-1159, 2007.

[7] R. Takahashi, H. Ise, A. Konno, M. Uchiyama, and D. Sato, 'Hybrid simulation of a dual-arm space robot colliding with a floating object', *Proceedings 2008 IEEE International Conference on Robotics and Automation*, pp. 1201-1206, 2008.

[8] K. Nagaoka, R. Kameoka, and K. Yoshida, 'Repeated Impact-Based Capture of a Spinning Object by a Dual-Arm Space Robot', *Frontiers in Robotics and AI*, Vol. 5, #115, 2018

[9] E. Rimon and A. Blake, 'Caging 2D Bodies by 1-Parameter Two-Fingered Gripping Systems', *Proceedings of the 1996 IEEE International Conference on Robotics and Automation*, pp. 1458-1464, 2018.

[10] Y. Umetani and K. Yoshida, 'Resolved Motion Rate Control of Space Manipulators with Generalized Jacobian Matrix', *IEEE Transactions on robotics and automation*, vol.5, no.3, pp.303-314, 1989.

[11] Z. Wang and V. Kumar, 'Object Closure and Manipulation by Multiple Cooperating Mobile Robots', *Proceedings 2002 IEEE International Conference on Robotics and Automation*, pp. 394-399, 2002.